Experimental and Computational Investigation of Particle Filtration Mechanisms in Partially Damaged DPFs

Onoufrios Haralampous, Marios Mastrokalos, Fotini Tzorbatzoglou, and Chris Dritselis

University of Thessaly

Abstract

Understanding the filtration mechanisms in partially damaged Diesel Particulate Filters is very important for the design of exhaust systems with efficient On-Board Diagnosis functionality, especially as new threshold limits have been recently applied for particulate mass leakage. Two common types of DPF failure are included in this study, namely rear plug removal and internal failure due to uncontrolled regeneration with excessive deposit loading. Initially, the two respective filters were loaded on the engine bench with particle measurement upstream and downstream, and then they were disassembled and sectioned to study the deposit distribution. The analysis of the second filter revealed several modes of failure that should be expected under real-life conditions such as material accumulation in the inlet channels, substrate melting, and crosswise and diagonal crack development. Moreover, a computational model with the necessary adjustments is used to simulate the loading experiments and interpret the underlying filtration mechanisms. The processed results reveal small effects of temperature and mass flow rate on the filtration efficiency and a comparatively stronger impact of the total deposit loading. The local deposit loading is uniform in the intact segments, while it is non-uniform with a minimum value at the failure location in the unplugged and internally damaged segments. This finding is consistent with the wall flow predicted by the model, whereas some discrepancies of the model can be attributed to a secondary collection mechanism.

Introduction

Since September 2018, new threshold limits are applied in the European Union for On-Board Diagnosis (OBD) of Particulate Mass (PM) leakage [1]. OBD systems are obliged to detect exhaust system malfunctions that account to 2.5 times higher PM emissions compared to the type approval limit. Often the malfunction is located in the Diesel Particulate Filter (DPF), which might suffer substrate crack or melting during harsh regeneration events. There are concerns that On-Board Diagnostic (OBD) systems are not always working effectively, which may allow environmentally-damaging component aging or failure to go undetected. Advanced diagnostic measures are necessary in the exhaust system to monitor the DPF filtration efficiency and tailpipe PM emissions. As a result, soot sensors have been developed for mass production and application in OBD systems [2, 3]

In addition, the European Union has recently focused research efforts on the development of exhaust systems more resilient to tampering [4].

DPF systems have been tampered with since many years because they can limit engine power, create maintenance problems, increase the consumption of fuel or simply because of the high cost of their replacement when they reach the end of their useful life or in case of malfunction. In this context, understanding the filtration mechanisms in partially damaged DPFs can facilitate the assessment of their environmental effects and the design of exhaust systems with efficient OBD functionality.

A common practice for failed DPF study is the artificial removal of rear plugs. Samaras et al. [5] and Finch et al. [6] used this approach to evaluate the limits of pressure sensing for OBD purposes. It was shown in these studies, that backpressure monitoring is not sufficient for on-board diagnosis of partially failed DPFs. Later reports [7, 8] employed modeling of partially damaged DPFs to access the amount of PM leakage and the applicability of soot sensor technology. The partially failed DPF models typically employ the classical Bissett and Shadman model [9, 10] with modified boundary conditions for the missing rear plugs [11], similar to partial wall-flow filters [12, 13]. Another approach suitable for internal cracks is to use very low wall flow resistance and zero filtration efficiency at the location of the failure. The underlying assumption in both these approaches is that particles follow the exhaust gas streamlines and are collected only when flow is diverged through the wall. Haralampous and Dritselis explored numerically both approaches in 2015 [14], calculating axial deposit profiles and evaluating the variation of filtration efficiency in the complete range of an engine map.

The main objective of the present study is the experimental validation of the aforementioned models in terms of deposit loading profile and the dependence of filtration efficiency on the mass flow rate, temperature and deposit loading. Furthermore, the models are tested under more realistic conditions, especially the DPF damaged during uncontrolled regeneration. Finally, the necessary model adjustments to predict the pressure drop and filtration efficiency with sufficient accuracy are discussed.

Engine-bench Testing

Three initially identical SiC substrates of typical size (5.66 in x 6 in) and cell geometry (300cpsi/12mil) were selected for testing. The first remained intact throughout the experimental procedure. The second denoted as "Unplugged" was manually damaged by trimming away the plugs in two central segments. The third DPF denoted as "Cracked" was subjected to an uncontrolled regeneration with high deposit

loading (19g/l), which resulted in a combination of failures including crack development and substrate melting.
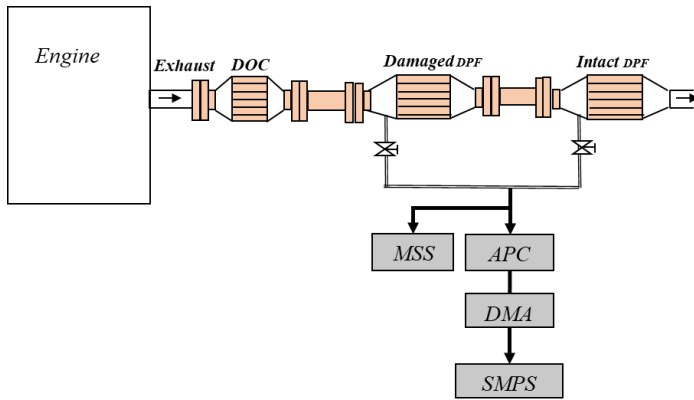

Figure 1. Engine bench experimental layout.

The test matrix included an uncontrolled regeneration and two loading tests, which were conducted at the Laboratory of Applied Thermodynamics/Aristotle University of Thessaloniki (LAT/AUTh), followed by disassembly of the DPFs and further analysis at the University of Thessaly in Larissa. The filters were installed on a Daimler 2.2l OM646 Diesel Engine and the particle emissions were characterized with a Micro Soot Sensor (MSS), an Airborne Particle Counter (APC), and a Scanning Mobility Particle Sizer (SMPS), using electronic vanes to sample upstream or downstream of the damaged DPF, as shown in Figure 1.

The loading protocol includes 4 phases:

1. Initial loading (1h)
2. Scanning at low deposit loading (1h)
3. Main loading (3h)
4. Scanning at medium deposit loading (1h)

Each scanning consists of four different engine operation points (A to D), specially selected to study the effect of mass flow rate and temperature. The exact conditions are summarized in Table 1.

Table 1. Engine operation points used in scanning procedure.

| Point	Mass Flow Rate [kg/h]	Temperature [°C]	EGR
Loading Phase	160	267	High
A	160	267	Normal
B	240	267	Normal
C	240	200	Normal
D	160	200	Normal

Data processing

As discussed above, the particle emissions were characterized in terms of soot mass and particle number concentration interchangeably upstream and downstream of the DPF. Thus, the raw signal had to be manually processed to extract a continuous time series for both locations. As an example, Figure 2a shows the raw and processed soot concentrations for the unplugged DPF. For the phases with only one

measurement, a constant value was used. For the main loading phase (2-5h), a linear profile was used. The initial loading phase (0-1h) exhibited a transient outlet concentration, which was approximated by more line segments. The drop of outlet soot concentration during the first 10 min is attributed to a respective inlet concentration variation, as expected due to the engine heat up. After that, the outlet concentration increases slightly, while the inlet concentration remains almost constant. Similar results are obtained for the particle number concentration, as shown in Figure 2b. The instantaneous filtration efficiencies for the particle mass (η_m) and number (η_{PN}) are readily available from the following relations:

$$\eta_m = 1 - \frac{c_{m,out}}{c_{m,in}} \qquad (1)$$

$$\eta_{PN} = 1 - \frac{c_{PN,out}}{c_{PN,in}} \qquad (2)$$
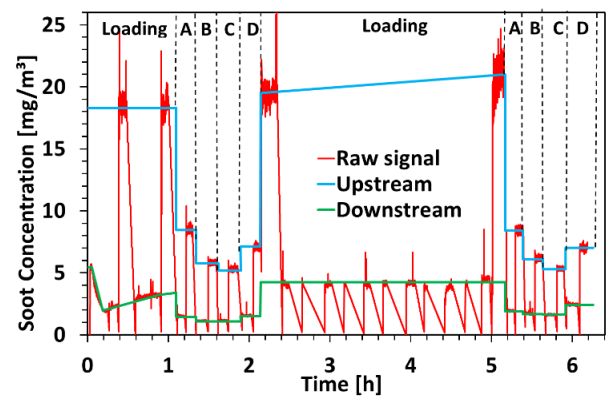
(a)
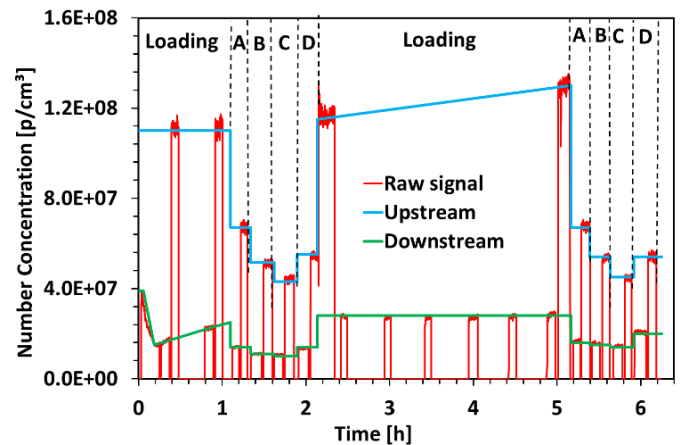
(b)

Figure 2. Raw and processed signals of (a) soot mass concentration and (b) particle number concentration for the loading of the unplugged DPF.

Two methods were used to estimate the cumulative mass filtration efficiency, shown in Table 2. Firstly, the initial and final DPF weights for each loading test were used to calculate the collected particulate mass in the DPFs and the filtration efficiency was estimated as:

$$\overline{\eta_m} = 1 - \frac{m_{d,intact}}{m_{d,total}} \qquad (3)$$

Secondly, the upstream and downstream instantaneous MSS emissions were integrated, resulting in the total and intact DPF soot mass, respectively. The soot mass in the damaged DPF was calculated as the difference between the two values. Again, the filtration efficiency was calculated by using Eq. (3). The two methodologies yield different results due to the different measurement principle. However, their ratio varies narrowly from 1.4 to 1.7, when the total values are considered. This observation is in accordance with Barba et al. [15], who found a mean ratio of 1.6 between CVS filter weighting and MSS integration for WLTC measurements downstream a DOC. More importantly, the present study indicates a reasonable agreement for the cumulative filtration efficiencies obtained by the two methodologies.

Table 2. Cumulative masses and efficiency estimated from weight difference and MSS signal integration.

Loading test	DPF	Weight difference [g]	MSS cum. mass [g]	Ratio [-]
Unplugged	Damaged	14.7	9.17	1.60
	Intact	4.8	2.38	2.02
	Total	19.5	11.56	1.69
	Efficiency[%]	75.4	79.2	0.95
Cracked	Damaged	11.9	7.66	1.55
	Intact	9.0	7.32	1.23
	Total	20.9	14.97	1.40
	Efficiency[%]	56.9	51.1	1.11

Deposit properties examination

To gain better understanding of the filtration mechanisms, the two compromised filters were disassembled and cut into pieces after the engine-bench loading. The ceramic monoliths were first sliced crosswise into several disks and then sectioned at the cement interface resulting in several blocks. Figure 3 shows the block naming convention with letters and numbers denoting disc and segment, respectively. The term segment in this study refers to the ceramic parts of complete filter length, as assembled by the manufacturer.

Figure 4a shows the rear face of the unplugged DPF after disassembly. The missing plugs can be identified in segments 23 and 32, as numbered from the frontal face. A representative intact segment (22) and a segment without plugs (23) were selected for further examination. Particulate matter is evident in the segments without plugs, but the rest of the segments are quite clean. Figure 4b presents the rear face of the cracked DPF. Black deposits can be observed in several outlet channels and a significant number of them are almost or completely blocked. Three representative segments at different locations, 23, 24 and 41 were selected to study the failure effects in the cracked DPF.

A high resolution camera (18 MP) was used to study the inlet and outlet face of the DPF blocks in these segments. Special care was given to align the camera to the channel axis. Figure 5 shows an image from the second block in the unplugged segment (B22). The deposit layer can be discerned as the dark material on the wall surface of the inlet channels. Additionally, some protrusions extend beyond the layer surface. Channels with rather uniform deposit layer and less protrusions were selected to measure the deposit layer thickness. At

03/29/2019

least three measurements were used to estimate a mean value, using the segment size as a reference.
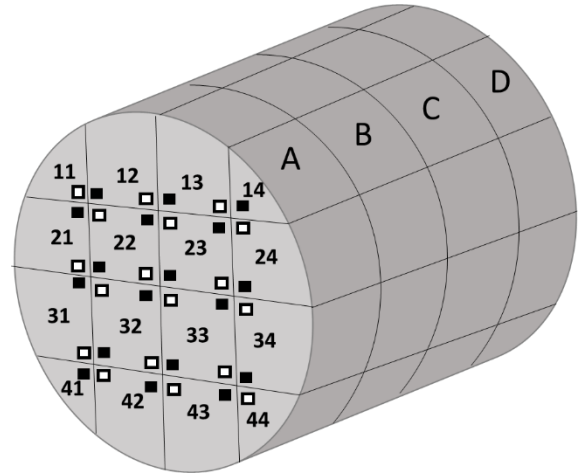

Figure 3. Naming convention of DPF blocks. Empty and full squares on frontal face denote inlet and outlet channels respectively.
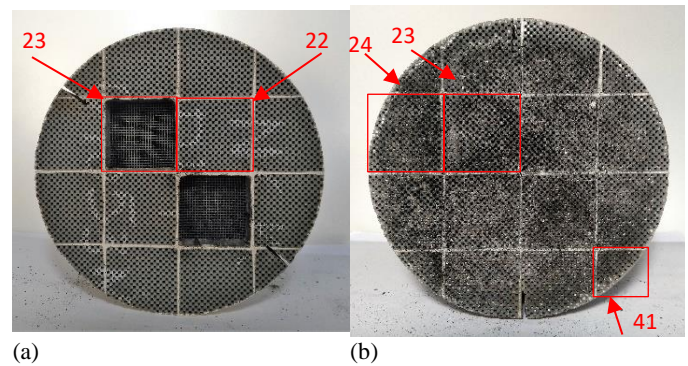

(a)   (b)

Figure 4. Rear faces of the two damaged DPFs and selected segments for further study: (a) unplugged DPF (b) cracked DPF.
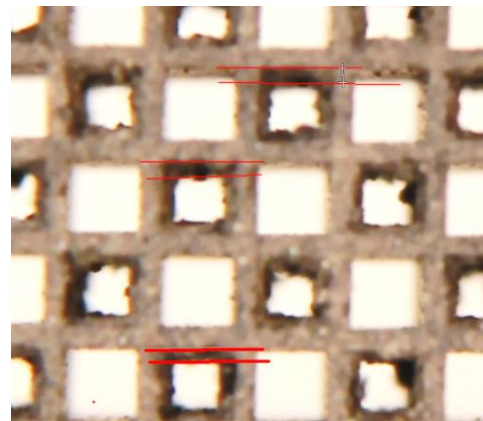

Figure 5. Frontal face of an intact segment (block B22) from the unplugged DPF. Marked distances were used to estimate deposit layer thickness.

The substrate blocks were weighted at loaded state using a high precision balance (Sartorius CPA64) with a readability of 0.1 mg. Beforehand, the blocks were heated for 30 min at 220 °C in a high temperature furnace (SNOL 1100) to minimize any humidity effects. A regeneration procedure followed with 1 h at 650 °C in the furnace to clean the blocks and weight them at clean state. Using the differential weight as the deposit mass and an estimated block volume, the local deposit concentration is calculated as:

$$\theta = \frac{m_{d,block}}{V_{block,eff}} \qquad (4)$$

In most cases, it was not possible to measure accurately the block volume due to uneven cuts, cracks or other faults. Hence, it was estimated from the regenerated block mass, using a well-shaped block as a reference:

$$V_{block,eff} = f_{eff} \frac{V_{ref}}{m_{ref}} m_{block} \qquad (5)$$

The periphery of the segments is covered with cement and the adjacent channels offer less area for deposit accumulation [16], so a correction coefficient f_{eff} equal to 0.92 was used to account for the inactive volume.

Figure 6 shows the schematic of an inlet channel with uniform deposit layer on the wall, as assumed by most computational models. Given the deposit layer thickness and the local deposit concentration, the deposit layer density can be estimated as:

$$\rho_d = \theta \frac{(d_c + w_w)^2}{2(d_c - w_d) w_d} \qquad (6)$$

The deposit layer thickness was measured both at the frontal and rear face of each block. The mean value that corresponds to the center of the block was used in Eq. (6) to comply with the deposit concentration at the same point.
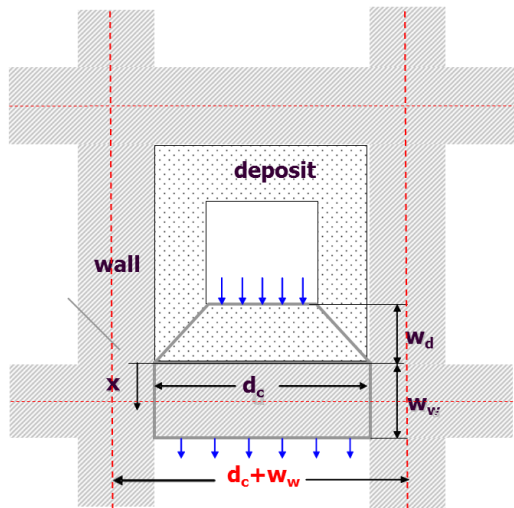

Figure 6. Schematic of a wall-flow DPF inlet channel.

Mathematical modeling

The fundamentals of wall-flow filter modeling were established in the early 1980s by Bissett and Shadman [9, 10]. Since then, DPF models have been refined and thoroughly validated [17, 18]. Here, only the differential equations used to calculate the flow field are presented in order to highlight the necessary model adjustments. The continuity and momentum balance are given for both inlet and outlet channel, denoted by the index i:

$$\frac{\partial}{\partial z}\left(\rho u_i d_h{}^2\right) = (-1)^i 4 d_h \rho u_w, \qquad i = 1,2 \qquad (7)$$

$$\frac{\partial p_i}{\partial z} + \frac{\partial}{\partial z}\left(\rho u_i{}^2\right) = -\frac{a_1 \mu u_i}{d_h{}^2}, \qquad i = 1,2 \qquad (8)$$

A Darcy expression is used for the pressure drop of the wall flow:

$$p_1 - p_2 = \frac{\mu u_w w}{k} \qquad (9)$$

with the term $\frac{w}{k}$ representing a hydrodynamic resistance of the wall and deposit layer.

The boundary conditions for the intact channel and the channel without rear plug are presented in Table 3.

Table 3. Boundary conditions of intact channel and inlet channel without rear plug [12, 13].

Intact channel	Channel without rear plug
$u_1(0) = u_{in}$ $u_2(0) = 0$ $u_1(L) = 0$ $p_2(L) = p_{out}$	$u_1(0) = u_{in}$ $u_2(0) = 0$ $p_1(L) = p_{out}$ $p_2(L) = p_{out}$

In the case of channels with internal faults, a very small hydrodynamic resistance $\frac{w}{k}$ is applied locally, along with zero wall filtration efficiency. Equivalent hydraulic networks are used to solve the flow field in the inlet and outlet channel, as well as the flow distribution between the segments as described in [18, 11]. Fault locations and modes are directly defined in the model based on experimental observations.

Results and Discussion

Unplugged DPF

The rear plugs were removed in two of the central segments of the unplugged DPF, as shown in Figure 4a. This corresponds to 14% of the total frontal area. Another 8% of the frontal area corresponds to the cement at the segment interfaces and the periphery. The experimental

and modeling results are presented alongside in this section. Several simulations are presented to discuss the necessary model adjustments.
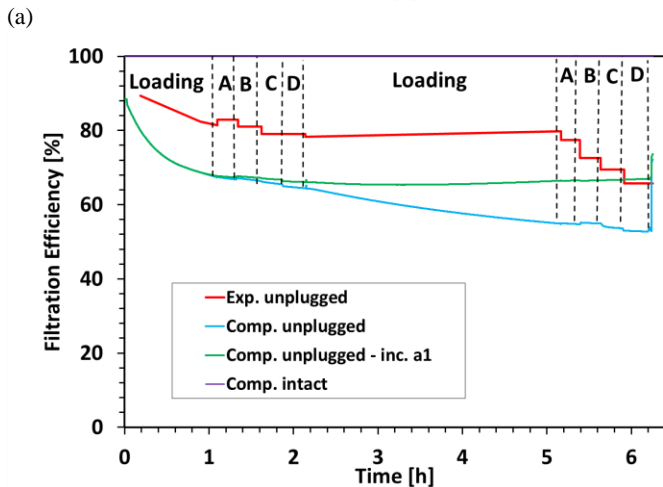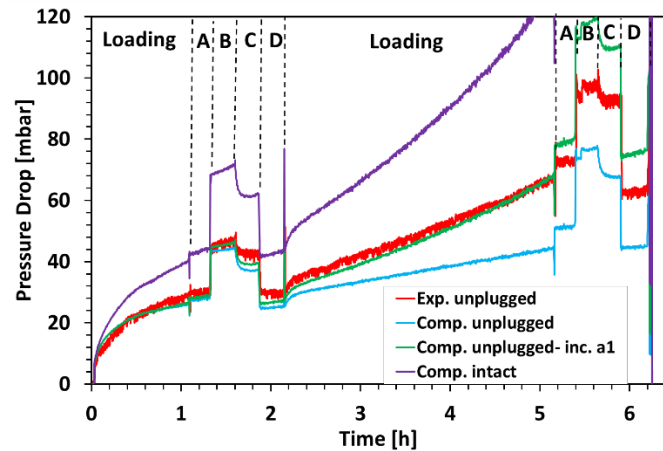

(a)

(b)

Figure 7. Pressure drop and mass-based filtration efficiency of unplugged DPF. Red line: experimental measurements, magenta line: computational results corresponding to intact filter, blue line: computational results without hydrodynamic factor, green line: computational results including hydrodynamic factor

Figure 7a depicts the evolution of pressure drop for the unplugged DPF. It is clearly lower than the pressure drop of the intact DPF, which is included in the same graph for reference. The initial prediction is very good regardless of the model calibration. The prediction of the pressure drop remains good for the initial loading phase and the first scanning, but deviates in the main loading phase. The backpressure gradient in the main loading phase seems to be rather high when compared to the measurements of Dabhoiwala et al. [19]. A preliminary sensitivity analysis, showed that the permeability of the deposit layer and substrate has small effect on the calculated pressure drop gradient. The governing phenomena for pressure drop take place in the open channels. In order to achieve good pressure drop prediction after the first 2h, an increased channel pressure coefficient a_1 was used. A possible explanation is that the layer roughness is not negligible and should be taken into account as explained by Kandlikar et al. [20]. In this case, transition to turbulent flow might take place at Reynolds numbers lower than the standard value. Moreover, porous walls can also lead to lower the critical Re number values [21]. In our case, the channel Re number reaches values of 1800 during the scanning phase in the vicinity of the unplugged channel entrance.

The respective experimental and computational filtration efficiency calculated from the MSS signal is shown in Figure 7b. The experimental value is very close to 80% throughout the loading, with the exception of the first and the second scanning phase. A gradual decrease is noticeable from point A to D. Similar trends are qualitatively predicted by the model, albeit at a lower level. Particle collection according to the model assumptions takes place both in the intact and damaged segments, as a fraction of the flow is forced through the wall. The rest of the flow leaks directly through the open channels, which essentially controls filtration efficiency. According to the model, the flow redistributes as the deposit accumulates, resulting in even lower efficiency. The sudden drop during the first 1h is related to the accumulation of deposit inside the wall pores. During the main loading phase, the experimental filtration efficiency remains almost constant, the original model shows a considerable drop, while the model with increased a_1 exhibits a similar behavior to the experimental one. In the latter case, the flow resistance increases at the same rate in the intact and unplugged segment, leading to a minimal redistribution. The discrepancy of the predicted filtration efficiency points out an additional collection mechanism that takes place in the open channels. Possible explanations could be the interception of particles at protrusions extending beyond the deposit layer and/or the turbulent flow in the channels.
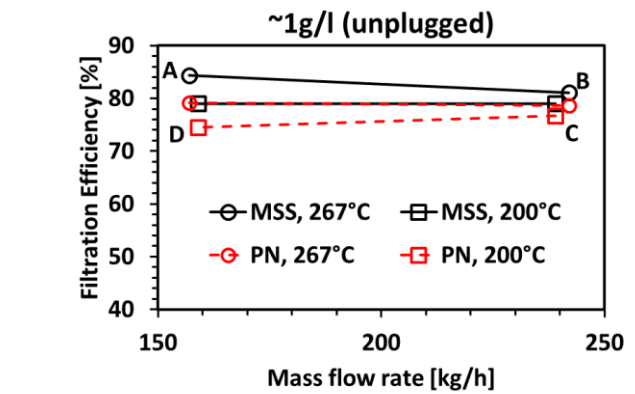
(a)
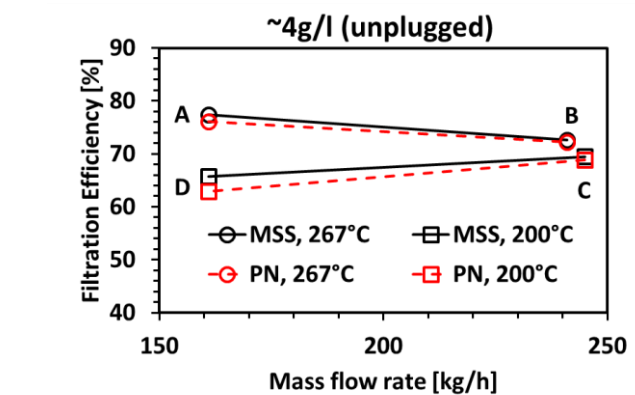
(b)

Figure 8. MSS derived filtration efficiency of the unplugged DPF as a function of mass flow rate and temperature for (a) low and (b) moderate deposit loading.

In order to investigate the effect of flow rate, temperature and deposit loading on the mass- and number-based filtration efficiencies, the processed values for the four scanning points are shown in Figure 8. Mass flow rate seems to have minimal effect on the efficiency, as indicated in both graphs. Efficiency increases weakly with

temperature, as shown by the comparison of results obtained at the two temperatures. It should be noted, that the increase of flow rate from point A to B is expected to cause some migration or restructuring of the loosely deposited particulate matter. This is consistent with the deviation between the experimental and calculated pressure drop at points B, C and D. Thus, the comparison focuses mostly on points B to D in order to avoid this effect. Similar trends are predicted by the model although to a lesser extent. The comparison of the two graphs suggests that the deposit loading accumulation from 1 to 4g/l results in a reduced efficiency of about 10 %. Interestingly, the FE values based on the particle number are consistently lower than those based on particle mass. This indicates that larger size particles are collected more efficiently than smaller. Again, this could be related to an additional filtration mechanism, besides surface filtration.

(a)

(b)

(c)

□ Plugged exp   —— Plugged comp
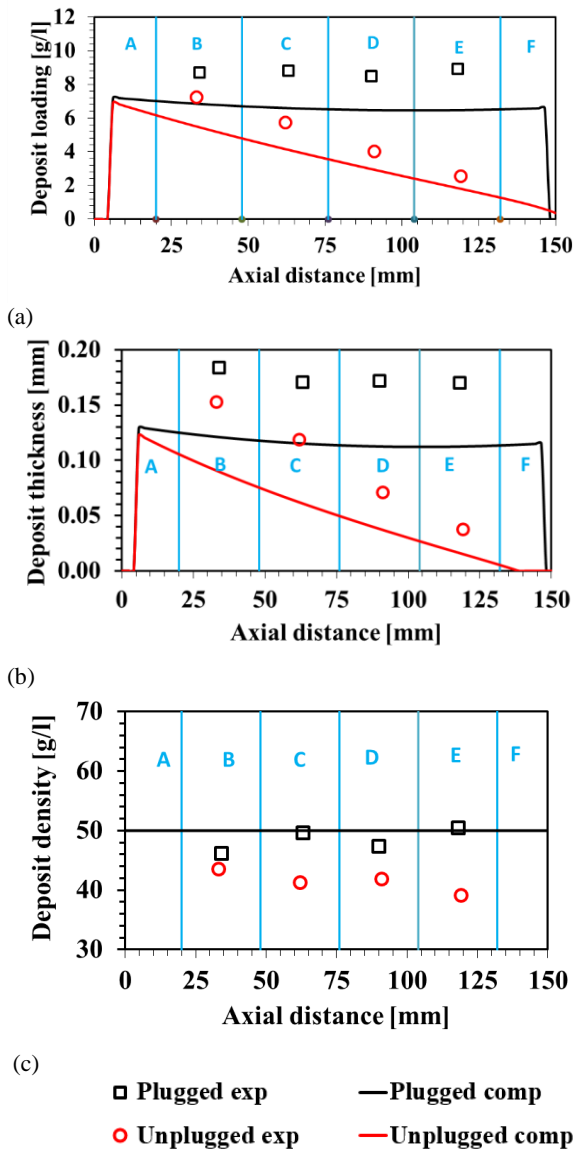
○ Unplugged exp   —— Unplugged comp

Figure 9. Intact and unplugged DPF segments: Profiles of (a) Soot loading, (b) soot thickness and (c) soot density.

Figure 9 shows the deposit properties profiles obtained from the experimental examination and the simulation. Only the results with the modified a_1 are presented, as all the simulations produced almost identical results. The first graph shows the deposit loading distribution

in the intact and unplugged segments. As the model underestimates filtration efficiency, the computational values are comparatively lower. More importantly, the deposit accumulates uniformly in the intact segment, while a linear profile with maximum value at the entrance and zero at the exit is evident in the unplugged segment. This kind of profile has been numerically predicted by Haralampous et al. [13, 11], but it is experimentally verified in the present study for the first time to the best of the authors' knowledge. The deposit thickness profiles shown in the second graph exhibits the same trends. Likewise the quantitative divergence of the experimental and computational profiles can be attributed to the lower filtration efficiency of the simulation in addition to slightly overestimated deposit density. By using the data from the first two graphs and Eq. (6), the deposit density profile can be obtained, which is shown in the third graph. A constant density profile close to a value of 50 kg/m³ is calculated for the intact segment, which confirms the validity of the experimental procedure. The profile is uniform also in the unplugged segment, but with a slightly smaller value. A uniform deposit density value has been used in the calculation for both segments.
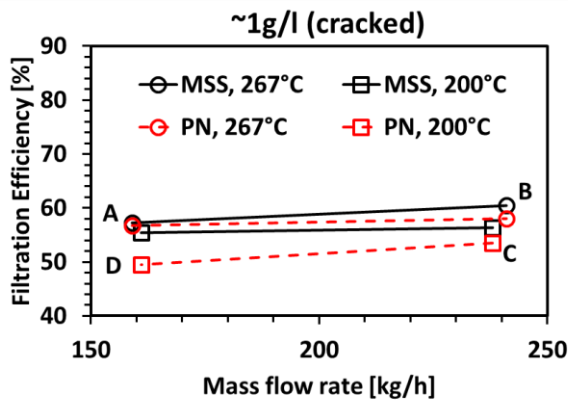
Cracked DPF

As shown in Table 2, the cracked DPF approached values of the cumulative efficiency close to 50%, revealing a more severe failure than the unplugged DPF. The cumulative efficiency is in agreement with the instantaneous efficiencies obtained from the MSS signal during the scanning phase. Furthermore, the dependence on the mass flow rate and temperature is rather small, as depicted in Figure 10. The number-based efficiency is again consistently lower than the mass-based. Interestingly, the small drop of efficiency from point A to B is not observed in this case.

The analysis of the cracked DPF revealed a more complex situation. Although denoted as cracked, several failure modes were identified in this filter. Furthermore, most of the segments contained a combination of intact and compromised channels.

Figure 11a and b respectively show the canning and DPF after disassembly. The insulating mat was partly destroyed and some of it had hardened and attached to the monolith periphery especially at the rear half of the filter periphery. Higher temperatures were attained in this location during the regeneration. Several ring-off cracks were evident on the monolith, mostly in the region of 2-5 cm from the entrance and secondly at 12-13 cm. Figure 11c shows the detail of a crack and the corresponding black mark on the mat from PM leakage. The width of the PM line on the mat hints to a rather small amount of exhaust gas leakage. A possible explanation is that leaked particles accumulate on the crack and block it shortly after the crack development.

Internal faults were revealed after the slicing of the cracked DPF. Figure 12a shows the inlet face of slice C, about 50 mm from entrance. Diagonal cracks are evident in most of the segments and about 50% of the central area has a lighter color than the periphery. A closer examination in this area shows a white material in the inlet channels, with some of them being completely blocked. Figure 12b shows the outlet face of section D, about 130 mm from entrance. This slice broke up during cutting and revealed extended substrate melting in the central and quadrilateral peripheral segments. This was combined with large diagonal cracks in many locations. Three segments from different locations were selected for further examination, as marked on the images. In addition, a plane in segment 24 was selected to inspect the interior of the channels.

(a)
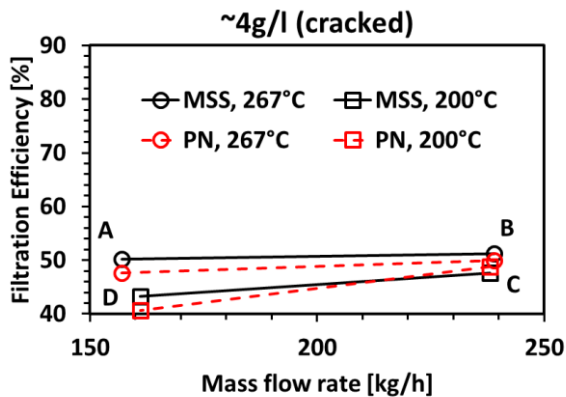
(b)

Figure 10. MSS derived filtration efficiency of the cracked DPF as a function of mass flow rate and temperature for (a) low and (b) moderate deposit loading.

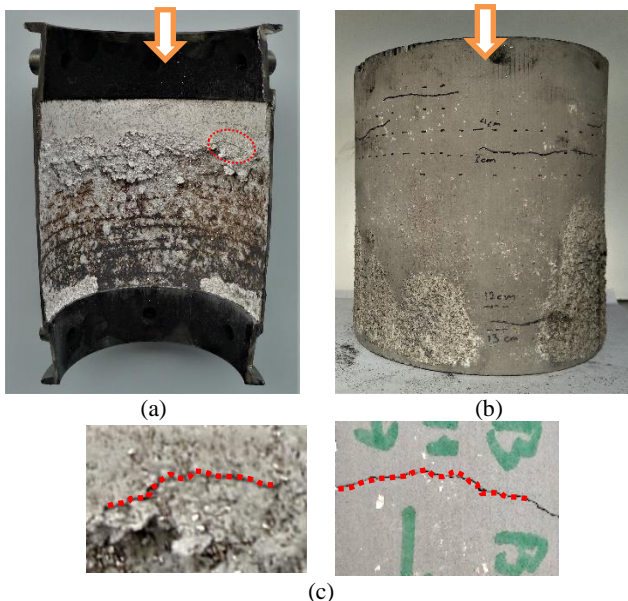

(a)   (b)

(c)

Figure 11. Images of the cracked DPF after disassembly showing (a) insulating mat failure, (b) cracks on the monolith periphery and (c) the detail of PM leak from the periphery to the insulating mat marked with a red line in both surfaces.

Figure 13 shows the state of inlet and outlet channels in this section. A light colored material is obvious inside the inlet channels, mostly in the form of a fractured layer. It should be noted that this DPF had not been used before this study and no ash accumulation was expected. The white material form and color is more or less similar upstream and downstream of the substrate melting. There is no evidence of the same material in the outlet channels, some of which have a distinct brownish color. This suggests that the unknown material accumulated in the inlet channels before the substrate melting. Moreover, the accumulation of this material was verified with the DPF weight, which was about 46g more than that expected after the uncontrolled regeneration. At the peak of the regeneration, exhaust gas temperatures reached as high as 750°C at the DOC outlet and 1400°C at the DPF. The origin of the material is still under investigation.
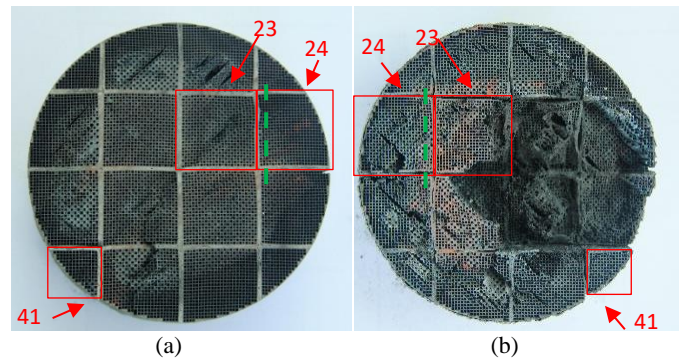

(a)   (b)

Figure 12. Images of the cracked DPF after slicing showing (a) diagonal cracks at the inlet face of slice C and (b) diagonal cracks and substrate melting on the outlet face of slice D. The segments marked with red squares were selected for further examination. The green line shows a plane discussed below.

Figure 13. Side of segment 24, slice C to E, showing the substrate melting and the internal of the channels after furnace regeneration.

Detailed results for the central segment are shown in Figure 14. Substrate melting is evident at the interface between blocks C and D. As a result, exhaust gas could flow freely from the inlet to the outlet channels, although in some cases the melted material blocked completely the channels. A maximum value of the deposit loading of 7 g/l was obtained near the entrance, while lower values appeared around the melting location. Similar results are shown in Figure 15 for segment 24. Block B was separated in two parts after the furnace regeneration, revealing an additional crack. It seems that this crack did not affect the local deposit concentration, which remained high. The minimum value is encountered in block D, where melting took place. The same trend was verified in the triangular segment (41). Substrate melting was observed in the marked area of segment D. In all cases, a minimum loading value is encountered at the melting location, while cracks do not seem to affect the profile.

Summing up, three failure modes were identified:

- Material accumulation in the inlet channels as a layer and a rear plug.
- Substrate melting resulting in inlet-outlet channel short-circuits and/or channel blocking.
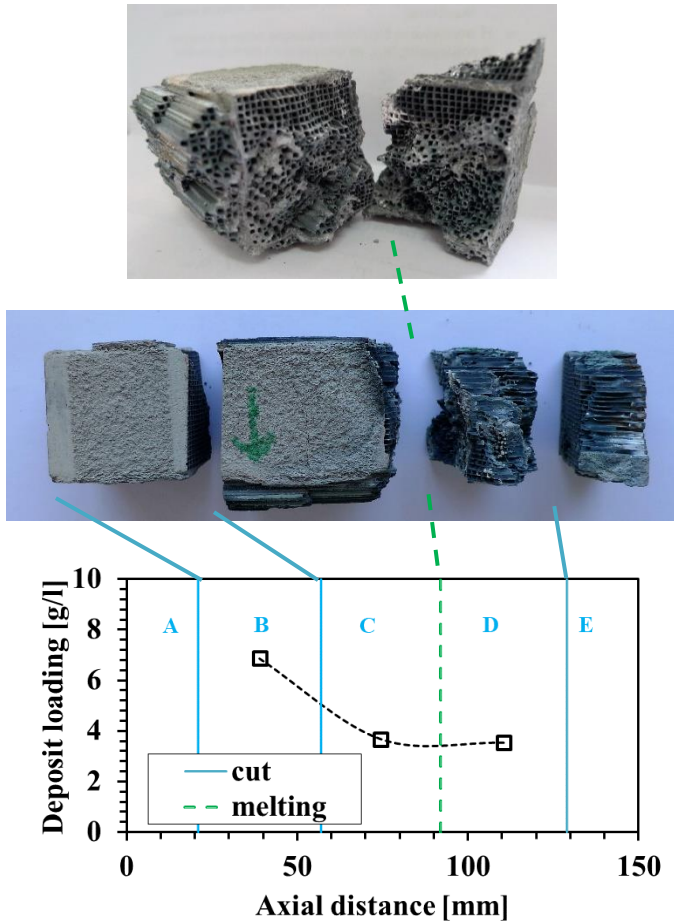- Crosswise and diagonal crack development.

Figure 14 Axial deposit distribution in central segment (23) of cracked DPF and images of the respective blocks.

Consequently, the DPF denoted as cracked presents a far more challenging modeling task. In order to account for these defects, the following assumptions were applied:

1. A coating was assumed on the surface of all inlet channels. This coating contributed both to the traverse flow resistance and the axial flow resistance due to cross-section area constriction. The pressure drop level of the damaged DPF at clean state provided a baseline for calibrating this parameter.
2. With the filtration efficiency in mind, 50% of the frontal area was considered failed. The inlet and outlet channels, which correspond to 25% of the area were assumed short-circuited. As explained in the model description, this was implemented as an insignificant wall flow resistance at the location of the failure, together with zero wall filtration efficiency.
3. The rest 25% failed area was assumed completely inaccessible to the flow. This could be attributed both to the material accumulation as a rear plug and the substrate melting. The local deposit concentration in the rest of the filter was used to verify this value.

03/29/2019

4. The leakage from most crosswise and diagonal cracks at the frontal half of the DPF was assumed insignificant. The rest was assumed to be covered by assumption 2.

This leaves 42% of the frontal area for intact inlet and outlet channels and 8% for area blocked by cement. The selected modeling approach, although simplified, facilitates the understanding of the filtration mechanisms.
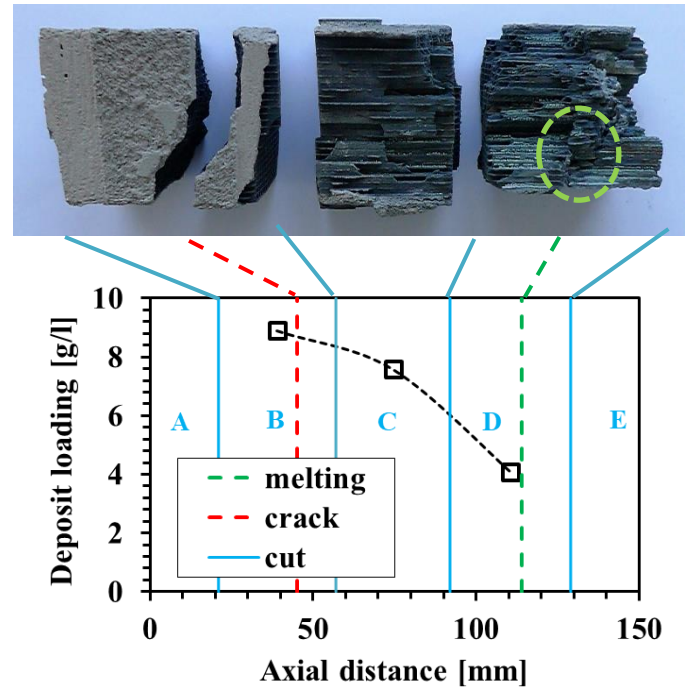

Figure 15. Axial deposit distribution in quadrilateral peripheral segment (24) of cracked DPF and images of the respective blocks.
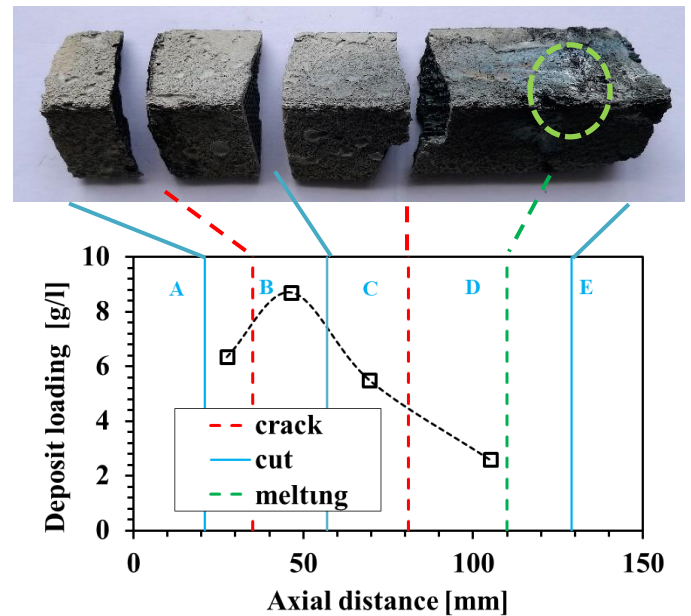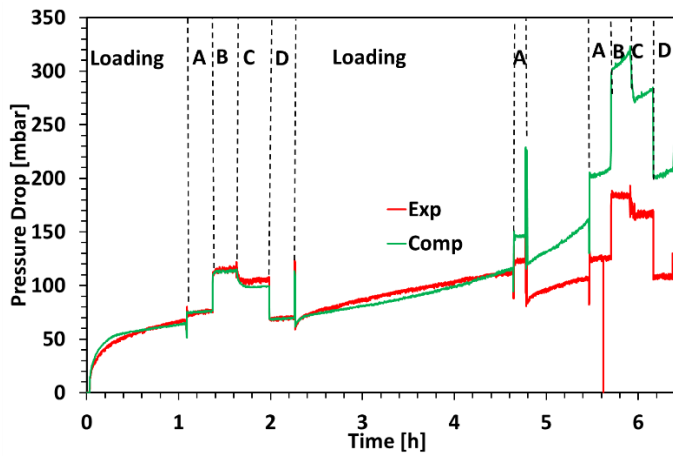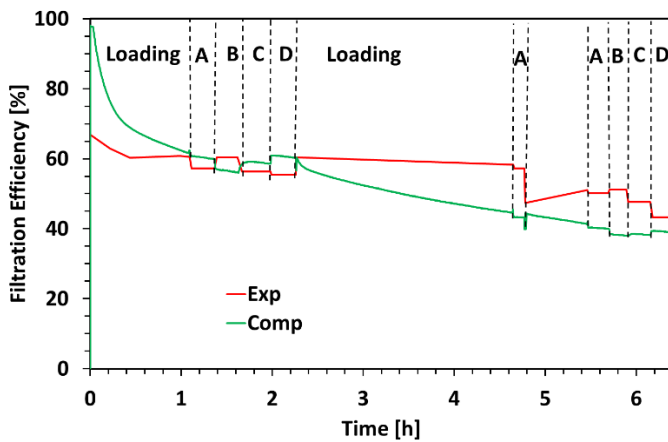

Figure 16. Axial deposit distribution in triangular peripheral segment (41) of cracked DPF and images of the respective blocks.

(a)

(b)

Figure 17. Pressure drop and mass-based filtration efficiency of cracked DPF. Red line: experimental measurements, green line: computational results.

Figure 17 shows the pressure drop and mass-based filtration efficiency obtained experimentally and computationally. A good agreement is evident for both magnitudes during the initial loading and the first scanning phase. Although not shown in the graph, the experimental pressure drop is actually higher than that of a hypothetical intact filter. The main loading starts at 2.2h and ends at 5.4h with an interruption at 4.6h. During the interruption, the engine operates at point A and for a few seconds it is further accelerated resulting in high flow rate. After this point, the experimental backpressure drops noticeably, while the computational is not affected. Deposit migration or restructuring inside the channel or at the melting location is again a possible explanation. It is worth mentioning, that the intact filter located downstream did not demonstrate this pressure drop discontinuity. In other words, if any deposit migration took place in the failed DPF, it didn't reach the intact filter. It is also interesting to note that the instantaneous efficiency dropped significantly at the same time. This efficiency drop is a manifestation of the same phenomenon that appeared in the unplugged DPF at the transition from point A to B. Additionally a non-linear experimental backpressure buildup is evident during the loading from 2.2 to 4.6h, which could be related to deposit properties variation.

Finally the numerical deposit profile for the intact segment and the segment with internal failure denoted as cracked is shown in Figure 18. It presents the same trend of a maximum loading at the entrance, which decreases closer to the melting location. The experimental

profiles shown in previous figures could be viewed as a combination of the intact and cracked profiles.
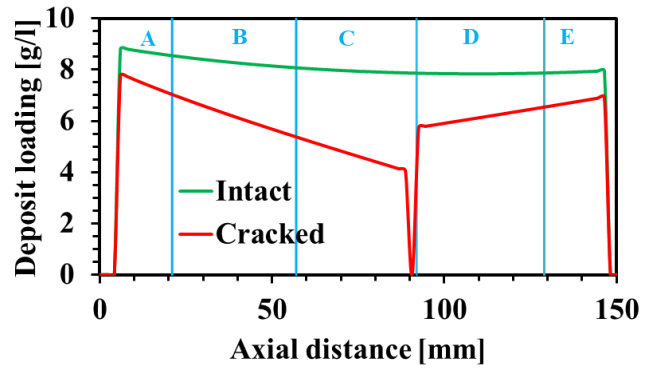

Figure 18. Cracked DPF: Computational profile of deposit loading for intact segment (green line) and cracked segment (red line).

Conclusions

It was experimentally verified that the main filtration mechanism in unplugged and internally damaged filters is due to particles following the exhaust gas streamlines. A fraction of the exhaust gas traverses through the wall both in the intact and damaged channels. Particles following these streamlines are collected on the wall due to surface filtration, resulting in profiles directly proportionate to the flow field. As a result, non-uniform linear deposit profiles appear in the damaged channels, characterized by a maximum value at the entrance and a close to zero value at the missing rear plug or the melting location. Smaller cracks have no effect on the deposit profile.

Indications of a secondary particle collection mechanism have been presented. This mechanism becomes apparent when the deposit has accumulated in the open unplugged channels and results in increased pressure drop and higher collection efficiency especially for the larger particles. A mechanism that fits this description is transition to turbulent flow due to the deposit layer roughness combined with interception of particles at the protrusions extending beyond the deposit layer. Also related to the latter is migration or restructuring of loosely-bonded deposit at the transition to higher flow rate. Similar phenomena are evident also in the internally damaged filter, although the critical location might be at the inlet-outlet channel short-circuit point. An advanced model is under development in order to take these phenomena into account.

Finally, it was concluded that DPF failure under real-life conditions can be considerably more complex than rear plug removal and combine material accumulation in the inlet channels, substrate melting and crosswise and diagonal crack development. In this case a number of assumptions have to be taken into account in the numerical model for sufficiently accurate simulations.

References

1. Commission Regulation (EU) No 459/2012 of 29 May 2012, Official Journal of the European Union L142/16.
2. Ntziachristos, L., Fragkiadoulakis, P., Samaras, Z., Janka, K. and Tikkanen, J. "Exhaust Particle Sensor for OBD Application," SAE paper 2011-01-0626, 2011.

3. Ochs, T., Schittenhelm, H., Genssle A. and Kamp B, "Particulate Matter Sensor for On Board Diagnostics (OBD) of Diesel Particulate Filters (DPF) ," SAE paper 2010-01-0307, 2010, doi:10.4271/2010-01-0307

4. EN Horizon 2020 Work Programme 2018-2020, 11. Smart, green and integrated transport, LC-MG-1-4-2018, "Hardening vehicle environmental protection systems against tampering," Oct 27, 2017

5. Samaras, Z., "On Board Diagnostics Legislation for Euro 6/VI Light and Heavy Duty Vehicles in Europe," On-Board Diagnostics Symposium, Indianapolis, USA, August 24-26, 2010.

6. Finch, S., Hnilicka, B. and Sindano, H., "EURO6 Light Duty Vehicle OBD Project: Evaluation and Assessment of Proposed EOBD Emission Thresholds," ACEA report Q51760, RD.10/320201.4, 2010.

7. Samaras, Z., Geivainidis, S., Vermeulen, R. et al., "Technical Feasibility of different regulatory OBD threshold limits (OTL) for Euro 6 (LD) vehicles," European Commission, DG Enterprise and Industry, Ref. Ares., 2015, doi:10.2769/32688

8. Kontses, D., "Soot emission model for real world operating conditions of a diesel engine car," Diploma Thesis, UIN: 4866 Aristotle University of Thessaloniki, 2014

9. Bissett, EJ. "Mathematical model of the thermal regeneration of a wall-flow monolith diesel particulate filter," Chem. Eng. Sci. 1984; 39 (7-8): 1233-1244.

10. Bissett, EJ and Shadman, F. "Thermal Regeneration of Diesel Particulate Monolithic Filters," AIChE Journal 1985, doi.org/10.1002/aic.690310508.

11. Haralampous, O., Mastellos, D., "A Multi-channel Mathematical Model For Partially Failed Diesel Particulate Filters," 8th GRACM, Volos, July 2015.

12. Basu, S., Henrichsen, M., Tandon, P., He, S. et al., "Filtration Efficiency and Pressure Drop Performance of Ceramic Partial Wall Flow Diesel Particulate Filters," SAE Int. J. Fuels Lubr. 6(3):877-893, 2013, doi:10.4271/2013-01-9072.

13. Haralampous, O., Kontzias T., "Approximate Pressure Drop and Filtration Efficiency Expressions for Semi-Open Wall-Flow Channels," Canadian Journal of Chemical Engineering, 92:1517-1525, 2014

14. Haralampous, O., Dritselis C., "Modeling of the loading in partially damaged DPFs," MODEGAT IV, Bad-Herrenalb, September 2015.

15. Barba, F., Vassallo, A., and Greco, V., "Estimation of DPF Soot Loading through Steady-State Engine Mapping and Simulation for Automotive Diesel Engines Running on Petroleum-Based Fuels," SAE Technical Paper 2017-24-0139, 2017, doi:10.4271/2017-24-0139

16. Koltsakis, G. C., Haralampous, O. A., Margaritis, N. K., Samaras Z. C., Vogt C.-D., Ohara E., Watanabe Y. and Mizutani T., "3-Dimensional Modeling of the Regeneration in SiC Particulate Filters," SAE Transactions: Journal of Fuels & Lubricants, SAE paper 2005-01-0953, Detroit, 2005, doi:10.4271/2005-01-0953.

17. Konstandopoulos, AG, Kostoglou, M, Vlachos, N. et al., "Advances in the Science and Technology of Diesel Particulate Filter Simulation," Advances in Chemical Engineering 2007, doi:10.1016/S0065-2377(07)33004-4

18. Koltsakis, G, Haralampous, O, Depcik C et al. "Catalyzed diesel particulate filter modeling," Rev Chem Eng 2013, doi:10.1515/revce-2012-0008

19. Dabhoiwala, R., Johnson, J., Naber, J., and Bagley, S., "A Methodology to Estimate the Mass of Particulate Matter Retained in a Catalyzed Particulate Filter as Applied to Active Regeneration and On-Board Diagnostics to Detect Filter Failures," SAE Technical Paper 2008-01-0764, 2008, doi:10.4271/2008-01-0764.

20. Satish, G. Kandlikar, Derek Schmitt, Andres L. Carrano, and James B. Taylor, "Characterization of surface roughness effects on pressure drop in single-phase flow in minichannels," Physics of Fluids 17, 100606, 2005

21. Suga, K., Matsumura, Y., Ashitaka Y., et al. "Effects of wall permeability on turbulence," Int J Heat Fluid Flow, 2010, doi:10.1016/2010.02.023

Contact Information

Associate Professor Onoufrios A. Haralampous,

University of Thessaly,

Tel: +30 2410 684546,

Email: onoufrios@uth.gr

Acknowledgments

Definitions/Abbreviations

Abbreviations

APC	Airborne Particle Counter
DMA	Differential Mobility Analyzer
DOC	Diesel Oxidation Catalyst
DPF	Diesel Particulate Filter
FE	Filtration Efficiency
MSS	Micro Soot Sensor
OBD	On-Board Diagnosis
PM	Particulate Mass
SMPS	Scanning Mobility Particle Sizer
WLTP	Worldwide Harmonised Light Vehicle Test Procedure

Variables

d_c	Clean channel width, m

d_h	Channel hydraulic diameter, m
f_{eff}	Effective volume coefficient, -
k	Permeability, m²
L	Monolith length, m
m	Mass, kg
p	Gas pressure, Pa
u	Velocity, m/s
V	Volume, m³
w	Layer thickness, m
z	Axial distance, m

Greek letters

a_1	Constant in channel pressure drop correlation, -
θ	Deposit concentration, kg/m³
η_m	Instantaneous mass-based filtration efficiency, -
$\overline{\eta_m}$	Cumulative mass-based filtration efficiency, -
η_{PN}	Instant. number-based filtration efficiency, -
μ	Exhaust gas viscosity, kg/m s
ρ	Density, kg/m³

Subscripts

d	Deposit layer
i	Channel index, 1=inlet, 2=outlet
in	Monolith inlet
out	Monolith outlet
w	Substrate wall

03/29/2019